Hindawi
Journal of Sensors
Volume 2018, Article ID 8526092, 10 pages
https://doi.org/10.1155/2018/8526092

Research Article

Steering Acoustic Intensity Estimator Using a Single Acoustic Vector Hydrophone

Guang Pu Zhang,[1,2,3] Ce Zheng,[1,2,3] and Wang Sheng Lin[4]

[1]*Acoustic Science and Technology Underwater Laboratory, Harbin Engineering University, Harbin 150001, China*
[2]*Key Laboratory of Marine Information Acquisition and Security (Harbin Engineering University), Ministry of Industry and Information Technology, Harbin 150001, China*
[3]*College of Underwater Acoustic Engineering, Harbin Engineering University, Harbin 150001, Heilongjiang, China*
[4]*Science and Technology on Sonar Laboratory, Hangzhou Applied Acoustics Research Institute, Hangzhou 310023, Zhejiang, China*

Correspondence should be addressed to Wang Sheng Lin; linwangshengwork@163.com

Received 17 April 2018; Revised 30 July 2018; Accepted 19 September 2018; Published 25 November 2018

Academic Editor: Armando Ricciardi

Azimuth angle estimation using a single vector hydrophone is a well-known problem in underwater acoustics. In the presence of multiple sources, a conventional complex acoustic intensity estimator (CAIE) cannot distinguish the azimuth angle of each source. In this paper, we propose a steering acoustic intensity estimator (SAIE) for azimuth angle estimation in the presence of interference. The azimuth angle of the interference is known in advance from the global positioning system (GPS) and compass data. By constructing the steering acoustic energy fluxes in the x and y channels of the acoustic vector hydrophone, the azimuth angle of interest can be obtained when the steering azimuth angle is directed toward the interference. Simulation results show that the SAIE outperforms the CAIE and is insensitive to the signal-to-noise ratio (SNR) and signal-to-interference ratio (SIR). A sea trial is presented that verifies the validity of the proposed method.

1. Introduction

Acoustic vector hydrophones (AVHs) employ a colocated sensor structure consisting of two or three orthogonally oriented velocity sensors and a pressure sensor [1–3]. The manifold structure suggests that AVHs have the following advantages over traditional pressure sensors: (1) they measure acoustic pressure as well as particle velocity at the sensor position and thus produce extra information for localization, and (2) the manifold is independent of the frequency of the source signal, which makes AVHs suitable for wideband source signals [4]. Because of these advantages, both the theoretical aspects and applications of AVHs have been widely studied over the last few decades.

An array of AVHs is introduced for multiple-source localization problems in [5]. A maximum-likelihood algorithm was developed in [6]. Conventional beamforming (Bartlett beamforming) and Capon beamforming (minimum-variance distortionless response beamforming) for two-dimensional direction of arrival (DOA) estimation using an array of AVHs were investigated in [7]. Subspace-based approaches such as MUSIC [8] and ESPRIT [9] have been applied to the localization problem. In [10], the authors proposed a method for underwater acoustic direction-finding using arbitrarily spaced AVHs.

Although the AVH array processing can provide better detection and estimation performance, these methods are computationally expensive and require consistency of each component of the pressure and particle velocity. Therefore, in some engineering applications, single-transmit single-receive (SISO) sonar systems, such as sonobuoys and other small-scale detection equipment, are widely used [11]. DOA estimation using a single vector sensor is investigated in [12–14]. In [12], the authors introduce an ESPRIT-based algorithm for azimuth and elevation estimation using a single vector hydrophone. A comparison of different techniques in

estimating the azimuth angle of a source is investigated in [13]. Given a single source with continuous spectrum against a background of isotropic and band-limited white Gaussian noise, azimuth angle estimation can be performed using a complex acoustic intensity estimator (CAIE, also known as an acoustic energy flux estimator), which is a maximum-likelihood detector, and an azimuth angle estimator that employs a single vector hydrophone, as discussed in [14]. The use of a complex acoustic intensity estimator is further discussed in [15–17]. In the presence of interference or multiple sources, the acoustic energy flux is a mixture of the signals from all the sources. Hence, a CAIE becomes ineffective unless the acoustic energy flux of each source can be separated out [17]. If the acoustic energy flux is separable in the frequency domain, a CAIE is applicable for azimuth angle estimation of multiple sources. However, it essentially relies on the difference in the frequency domain. It is unable to distinguish the azimuth angles of multiple sources when the acoustic energy fluxes overlap in the frequency domain.

In this paper, we propose an efficient azimuth angle estimation method for a source of interest in the presence of interference. The azimuth angle of interference is assumed to be known from the global positioning system (GPS) and compass data. Taking advantage of acoustic energy flux characteristics in the spatial domain, we construct two variables of acoustic energy flux in the x and y channels of the AVH, defined as the steering acoustic energy flux. Thus, the azimuth angle of interest can be obtained when the steering azimuth angle is directed toward the interference. Simulations verify that this method can estimate the azimuth angle of interest accurately against the background of interference. Moreover, it is computationally inexpensive, requiring only simple multiplication and division operations plus fast Fourier transformation (FFT). In contrast to traditional approaches, matrix inversion is not required and the FFT is based on a fast algorithm.

The remainder of this paper is organized as follows. In Section 2, the AVH signal model and steering acoustic intensity estimator are introduced. Simulations are presented in Section 3. Section 4 presents the estimation results and an analysis of a sea trial in the South China Sea. Finally, conclusions are drawn in Section 5.

2. Steering Acoustic Intensity Estimator

Estimation using an AVH is based on analysis of three velocity components located at the origin of a three-dimensional space, with coordinates x, y, and z. Let $\mathbf{v}(\mathbf{r}, t) \in \mathbb{R}^{3\times 1}$ denote the particle velocity of an acoustic wave at position $\mathbf{r}$ in three-dimensional space, and let $p(\mathbf{r}, t) \in \mathbb{R}$ be the acoustic pressure. The relation between the acoustic pressure and the particle velocity is obtained from Euler's equation [18] and is given by

$$\mathbf{v}(\mathbf{r}, t) = -\frac{p(\mathbf{r}, t)}{\rho_0 c}\mathbf{u}(t), \tag{1}$$

where ρ_0 and c are the ambient pressure and the speed of sound in the medium. $\mathbf{u}(t)$ is the unit vector pointing from the origin toward the source position, given by

$$\mathbf{u}(t) \triangleq \begin{bmatrix} \cos(\theta)\cos(\phi) \\ \cos(\theta)\sin(\phi) \\ \sin(\theta) \end{bmatrix}, \tag{2}$$

where $\theta \in (-\pi, \pi]$ and $\phi \in [-\pi/2, \pi/2]$ denote the azimuth angle and the elevation angle, respectively. We consider two statistically independent broadband plane waves, traveling in an isotropic, quiescent, homogeneous fluid medium and impinging on a single AVH. Only the azimuth angle θ is considered in this paper, and the elevation angle is neglected. The unit vector then becomes

$$\mathbf{u}(t) \triangleq \begin{bmatrix} \cos(\theta) \\ \sin(\theta) \end{bmatrix}. \tag{3}$$

Hence, the two plane waves are parameterized by their respective azimuth angles θ_1 and θ_2. Source 1 is considered as the interference, and its azimuth angle θ_1 is known in advance from GPS and compass data. Then, θ_2 is the azimuth angle of interest. The received-signal model can be written as

$$\mathbf{y}(t) = \sum_{i=1}^{2} \begin{bmatrix} 1 \\ -\frac{1}{\rho_0 c}\mathbf{u}_i(t) \end{bmatrix} p_i(\mathbf{r}, t) + \begin{bmatrix} \mathrm{n_p}(t) \\ \mathbf{n_v}(t) \end{bmatrix}, \tag{4}$$

for sources $i = 1, 2$. Here, $n_{\mathrm{p}}(t) \in \mathbb{C}$ and $\mathbf{n}_{\mathrm{v}}(t) \in \mathbb{C}^{2\times 1}$ represent the corresponding pressure and velocity noise terms, respectively. We assume (i) that the noise terms in (4) are independent and identically distributed (i.i.d.), zero-mean complex circular Gaussian processes and are independent of the different channels and (ii) that the source signal and the noise are independent. The location of the AVH, $\mathbf{r}$, which is known and fixed at all time steps, can be omitted from these variables. Thus, the mathematical expressions for the different channels can be written as

$$\begin{aligned} p_i(t) &= p_i(\mathbf{r}, t), \\ v_{x,i}(t) &= -\frac{1}{\rho_0 c} p_i(t)\cos(\theta_i), \\ v_{y,i}(t) &= -\frac{1}{\rho_0 c} p_i(t)\sin(\theta_i), \end{aligned} \tag{5}$$

for sources $i = 1, 2$. Equation (4) can be simplified as

$$\mathbf{y}(t) = \sum_{i=1}^{2} \mathbf{x}_i(t) + \mathbf{n}(t), \tag{6}$$

where $\mathbf{x}_i(t) = [p_i(t), v_{x,i}(t), v_{y,i}(t)]^T$ and $\mathbf{n}(t) = [\mathrm{n}_p(t), \mathbf{n}_v(t)]^T$, and superscript T denotes the matrix transpose. On applying

an FFT to $\mathbf{y}(t)$, the received signal at frequency w can be written as

$$\mathbf{y}(w) = \sum_{i=1}^{2} \mathbf{x}_i(w) + \mathbf{n}(w). \tag{7}$$

The covariance matrix of the received signal can be expressed as

$$\mathbf{R} = \mathbb{E}\left\{\mathbf{y}(w)\mathbf{y}(w)^H\right\} = \sum_{i=1}^{2} P_i \mathbf{a}(\theta_i)\mathbf{a}^H(\theta_i) + \mathbf{R}_{\mathrm{n}} = \begin{bmatrix} R_{11} & R_{12} & R_{13} \\ R_{21} & R_{22} & R_{23} \\ R_{31} & R_{32} & R_{33} \end{bmatrix} \tag{8}$$

where superscript H denotes the conjugate transpose. P_i denotes the acoustic intensity of source i, and $\mathbf{R}_{\mathrm{n}}$ denotes the noise intensity, given by

$$P_i = \mathbb{E}\left\{p_i(w)p_i^H(w)\right\}, \tag{9}$$

$$\mathbf{R}_{\mathrm{n}} = \begin{bmatrix} I_{np} & 0 & 0 \\ 0 & I_{nx} & 0 \\ 0 & 0 & I_{ny} \end{bmatrix}, \tag{10}$$

$$\mathbf{a}(\theta_i) = \begin{bmatrix} 1 \\ \cos(\theta_i) \\ \sin(\theta_i) \end{bmatrix}, \tag{11}$$

$$\mathbf{a}(\theta_i)\mathbf{a}^H(\theta_i) = \begin{bmatrix} 1 & \cos(\theta_i) & \sin(\theta_i) \\ \cos(\theta_i) & \cos^2(\theta_i) & \cos(\theta_i)\sin(\theta_i) \\ \sin(\theta_i) & \sin(\theta_i)\cos(\theta_i) & \sin^2(\theta_i) \end{bmatrix}. \tag{12}$$

Substituting (10) and (12) into (8), the individual elements of the covariance matrix can be given as

$$R_{11} = P_1 + P_2 + I_{np}, \tag{13}$$

$$R_{22} = P_1\cos^2(\theta_1) + P_2\cos^2(\theta_2) + I_{nx}, \tag{14}$$

$$R_{33} = P_1\sin^2(\theta_1) + P_2\sin^2(\theta_2) + I_{ny}, \tag{15}$$

$$R_{12} = R_{21} = P_1\cos(\theta_1) + P_2\cos(\theta_2), \tag{16}$$

$$R_{13} = R_{31} = P_1\sin(\theta_1) + P_2\sin(\theta_2), \tag{17}$$

$$R_{23} = R_{32} = P_1\sin(\theta_1)\cos(\theta_1) + P_2\sin(\theta_2)\cos(\theta_2). \tag{18}$$

We construct two variables $\mathcal{I}_x(\theta_1, \theta_2, \theta)$ and $\mathcal{I}_y(\theta_1, \theta_2, \theta)$ based on the covariance matrix of the received signal and defined as the steering acoustic energy fluxes of the x and y channels, respectively, given by

$$\mathcal{I}_x^2(\theta_1, \theta_2 \mid \theta) = \left|\frac{R_{22} - R_{12}\cos(\theta) - I_{nx}}{R_{33} - R_{13}\sin(\theta) - I_{ny}}\right|, \tag{19}$$

$$\mathcal{I}_y^2(\theta_1, \theta_2 \mid \theta) = \left|\frac{R_{23} - R_{13}\cos(\theta)}{R_{23} - R_{12}\sin(\theta)}\right|, \tag{20}$$

where θ denotes the steering azimuth angle. The purpose of defining these two expressions is to derive an analytic solution that contains the relationship between θ_1 and θ_2. These definitions are obtained through reverse derivation. The azimuth angle of interference can be estimated from the GPS and compass data, denoted as $\widehat{\theta}_1$. The steering azimuth angle is directed toward the estimated azimuth angle, given as $\theta = \widehat{\theta}_1$. Moreover, the steering azimuth angle is assumed in the neighborhood of the interference $\widehat{\theta}_1 \approx \theta_1$. Substituting the elements of covariance matrix from (13), (14), (15), (16), (17), and (18) into (19) and (20), we have

$$\mathcal{I}_x^2(\theta_1, \theta_2 \mid \theta)\big|_{\theta=\widehat{\theta}_1} = \left|\left[\frac{\sin(\theta_2)}{\cos(\theta_2)}\right]^{-1} \frac{\cos(\theta_2) - \cos\left(\widehat{\theta}_1\right)}{\sin(\theta_2) - \sin\left(\widehat{\theta}_1\right)}\right|, \tag{21}$$

$$\mathcal{I}_y^2(\theta_1, \theta_2 \mid \theta)\big|_{\theta=\widehat{\theta}_1} = \left|\left[\frac{\sin(\theta_2)}{\cos(\theta_2)}\right] \frac{\cos(\theta_2) - \cos\left(\widehat{\theta}_1\right)}{\sin(\theta_2) - \sin\left(\widehat{\theta}_1\right)}\right|. \tag{22}$$

Straightforward derivations are given in the appendix. Thus, we obtain an estimate of θ_2 in the form of its tangent, given by

$$\tan^2(\theta_2) = \frac{\mathcal{I}_y^2(\theta_1, \theta_2 \mid \theta)\big|_{\theta=\widehat{\theta}_1}}{\mathcal{I}_x^2(\theta_1, \theta_2 \mid \theta)\big|_{\theta=\widehat{\theta}_1}}. \tag{23}$$

Intuitively, we can estimate θ_2 by an arctangent estimator based on the steering acoustic energy fluxes and called the steering acoustic intensity estimator (SAIE), which is given by

$$\theta_2 = \tan^{-1}\left\{\pm\frac{\mathcal{I}_y\left(\widehat{\theta}_1\right)}{\mathcal{I}_x\left(\widehat{\theta}_1\right)}\right\}, \tag{24}$$

where $\mathcal{I}_y(\widehat{\theta}_1) = {}^{\text{abbr.}}\, \mathcal{I}_y(\theta_1, \theta_2 \mid \theta)\big|_{\theta=\widehat{\theta}_1}$ and $\mathcal{I}_y(\widehat{\theta}_1) = {}^{\text{abbr.}}\, \mathcal{I}_y(\theta_1, \theta_2 \mid \theta)\big|_{\theta=\widehat{\theta}_1}$. As we can see, the form of the SAIE is similar to that of a conventional acoustic intensity estimator [17]. As we can see, multiple estimates of the azimuth angle θ_2 can be obtained using (24), not all of which are correct. False values can be eliminated by inserting θ_2 into (8).

Related to (19) and (20), we need to estimate the azimuth angle of interference, $\widehat{\theta}_1$, and the noise intensities related to

the x and y channels, $\widehat{I}_{nx}$ and $\widehat{I}_{ny}$. Assuming that the noise terms are stationary and that interference exists at all time steps, we can obtain estimates of the noise intensity before the source of interest appears, which are given by

$$\begin{aligned}\widehat{I}_{nx} &= \langle v_x(w)v_x^*(w)\rangle - \langle p(w)v_x^*(w)\rangle \cos\left(\widehat{\theta}_1\right),\\ \widehat{I}_{ny} &= \left\langle v_y(w)v_y^*(w)\right\rangle - \left\langle p(w)v_y^*(w)\right\rangle \sin\left(\widehat{\theta}_1\right),\end{aligned} \tag{25}$$

where $*$ denotes the complex conjugate. It is worth mentioning that there are errors when estimating the parameters $\widehat{\theta}_1$, $\widehat{I}_{nx}$, and $\widehat{I}_{ny}$. Considering the estimation errors of these parameters, the performance of SAIE will be presented in the next section.

In the case where two sources are present, SAIE can give an estimate of θ_2 with high precision. From (21) and (22), $\theta_2 = \theta_1$ and $\pi - \theta_1$ are the singular points of $\mathcal{J}_x$, and $\theta_2 = \pm\theta_1$ are the singular points of $1/\mathcal{J}_x$. The area in the neighborhood of $\pm\theta_1$ and $\pi - \theta_1$ is defined as the singular area. When the source of interest is located in the singular area, noise fluctuations can have a strong influence on the acoustic energy flux, causing the performance of SAIE to deteriorate rapidly.

3. Simulations

In this section, several experiments are presented to investigate the performance of the SAIE method in the presence of interference with different powers and azimuth angles of acoustic sources.

Source 1 is the interference and source 2 is the source of interest. These two sources are generated with broadband continuous spectra. The integration time is 1 second. The performance is evaluated over 500 Monte Carlo runs. The unit of estimation in all figures presented here is the degree (°).

3.1. Performance for Different SNR and SIR. The interference is located at $\theta_1 = 120^\circ$ and the source of interest at $\theta_2 = 30^\circ$. Figure 1 presents the performance of estimation of the azimuth angle of source 2, θ_2, with Figure 1(a) corresponding to the mean signed deviation (MSD), defined as

$$\text{MSD} = \sum_{j=1}^{J} \frac{\widehat{\theta}_2^{(j)} - \theta_2}{J}, \tag{26}$$

where $\widehat{\theta}_2^{(j)}$ is the jth estimate of the azimuth angle of interest and $J = 500$ is the times of Monte Carlo runs.

Figure 1(b) presents the root mean square deviation (RMSD), defined as

$$\text{RMSD} = \sqrt{\sum_{j=1}^{J} \frac{\left(\widehat{\theta}_2^{(j)} - \theta_2\right)^2}{J}}. \tag{27}$$

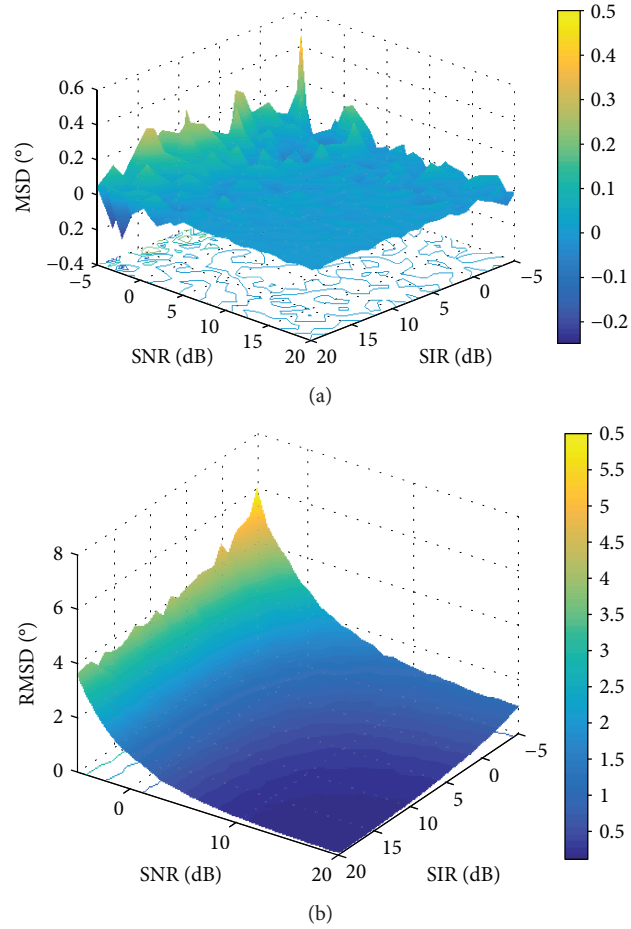

Figure 1: Performance of SAIE for different SNR and SIR: (a) MSD and (b) RMSD.

As we can see, SAIE is unbiased when the SNR and SIR are greater than 0 dB. As the SNR and SIR increase, the estimated RMSD begins to decrease. Related to Figure 1(b), RMSD equals to 1° when SNR = 20 dB and SIR = −5 dB while RMSD equals to 4° when SNR = −5 dB and SIR = 20 dB. The proposed SAIE method performs better in low SIR. In other words, it is more sensitive to SNR.

3.2. Performance versus Estimation Errors of Steering Azimuth Angle and Noise Intensities. Again, the interference is located at $\theta_1 = 120^\circ$ and the source of interest at $\theta_2 = 30^\circ$. SNR = 5 dB and SIR = 10 dB. As mentioned in Section 2, we need the estimated azimuth angle of interference, $\widehat{\theta}_1$, corresponding to the steering azimuth angle θ and the estimated noise intensities related to the particle velocity channels $\widehat{I}_{nx}$ and $\widehat{I}_{ny}$, as priors of SAIE. However, there are errors when estimating these parameters. Monte Carlo experiments are carried out to simulate the influence of the parameters $\widehat{\theta}_1$, $\widehat{I}_{nx}$, and $\widehat{I}_{ny}$, as shown in Figure 2, with Figure 2(a) corresponding to the error in $\widehat{\theta}_1$, given by $|\widehat{\theta}_1 - \theta_1|$, and Figure 2(b) corresponding to the percentage error in $\widehat{I}_{nx}$ and $\widehat{I}_{ny}$, given by $|\widehat{I}_{nx} - I_{nx}/I_{nx}| \times 100\%$, and similarly for $\widehat{I}_{ny}$.

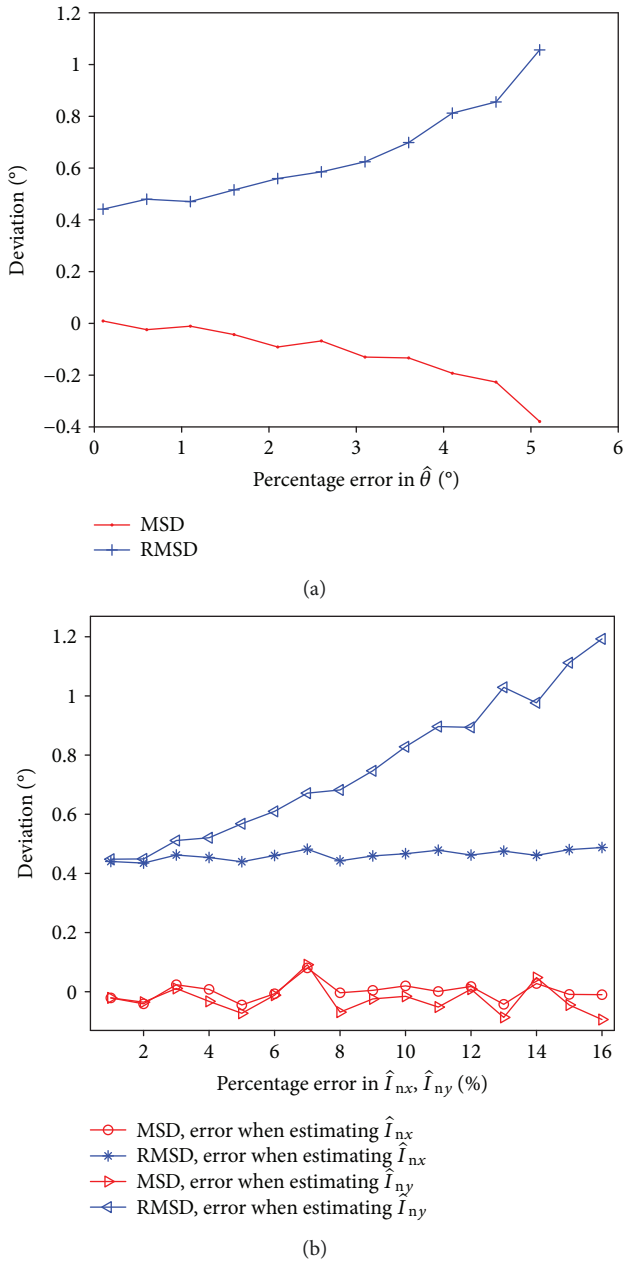

FIGURE 2: Performance of SAIE versus estimation errors of steering azimuth angle $\widehat{\theta}_1$ and noise intensities $\widehat{I}_{nx}$ and $\widehat{I}_{ny}$. (a) Error in $\widehat{\theta}_1$ and (b) percentage error in $\widehat{I}_{nx}$, $\widehat{I}_{ny}$.

As we can see, the MSD and RMSD increases when the error in $\widehat{\theta}_1$ increases. The RMSD increases more rapidly when the error in $\widehat{I}_{ny}$ increases, compared with the error in $\widehat{I}_{nx}$. In other words, the SAIE method is more sensitive to the error in $\widehat{I}_{nx}$.

3.3. Singular Area. As mentioned in Section 2, the performance of SAIE deteriorates rapidly when the source of interest is located in the singular area. Figure 3 presents the performance of SAIE for different localizations of the interference θ_1 at SNR = 5 dB and SIR = 10 dB. Figures 3(a) and 3(b) show the MSD, with Figure 3(b) being the planform of Figure 3(a). Figures 3(c) and 3(d) show the RMSD, with Figure 3(d) being the planform of Figure 3(c). As we can see, the SAIE method is able to estimate the azimuth angle of interest in most regions. When the source of interest enters the singular area of the steering acoustic energy flux, i.e., $\pm\theta_1$ and $180 - \theta_1$, the SAIE method becomes biased. When the interference azimuth angle satisfies $\theta_1 = \pm 180$ or 0, singular areas gather in one region. In the nonsingular area, the RMSD is less than 0.5°.

3.4. Simulation on a Typical Distributed Passive Localization System. Recent advances in distributed sensors providing unprecedented capabilities for target detection and localization have motivated the deployment of sensor networks for acoustic source detection and localization [19, 20]. A typical distributed passive localization system consisting of four buoys with star symbols is shown in Figure 4. A single AVH is mounted on each buoy. The deployments of the four buoys are 1# (−1500, −1500)m, 2# (1500, −1500)m, 3# (1500, 1500)m, and 4# (−1500, 1500)m, respectively. The red line corresponds to the true track of the source of interest and the magenta line to the true track of a moving interference. SNR = 5 dB and SIR = 10 dB. The time between each frame is T = 0.5 s.

Figure 5 shows the estimation results for buoys 2# and 3#, respectively. Blue points and green points correspond to the estimation results from CAIE and SAIE, respectively. Red points and magenta points correspond to the true tracks of the source of interest and interference, respectively. The CAIE method is obviously invalid in the presence of interference. However, SAIE is able to localize the azimuth angle accurately and consistently lock on to the true trajectory.

Figure 6 shows the tracking result from a typical distributed passive localization system. Firstly, the azimuth angle of source 2 was estimated using both SAIE and CAIE. Subsequently, the weighted least-squares (WL) algorithm was applied to triangulate the DOAs and obtain two-dimensional location parameters. The blue points are the tracking results using the estimates obtained from the CAIE method as the input, and the green points are the tracking results using the estimate obtained from the SAIE method. The red line is the true track of source 2.

4. Sea Trial Analysis

In April 2011, we conducted a sea trial in the South China Sea to compare the performance of CAIE and SAIE in the presence of a moving interference. A typical distributed passive localization system consisting of six buoys with star symbols is shown in Figure 7. Each buoy had a single AVH mounted on it and was fixed. The red line is the true track of ship 2, which was used as the base station and signal processing center. The magenta line is the true track of ship 1, which was used as the relay station. These tracks were obtained from GPS data. Ship 2 was floating with its engine turned off and towed a low-frequency acoustic source, namely, source 2. Ship 1 moved at a speed of 4 knots and towed a high-frequency acoustic source, namely, source 1.

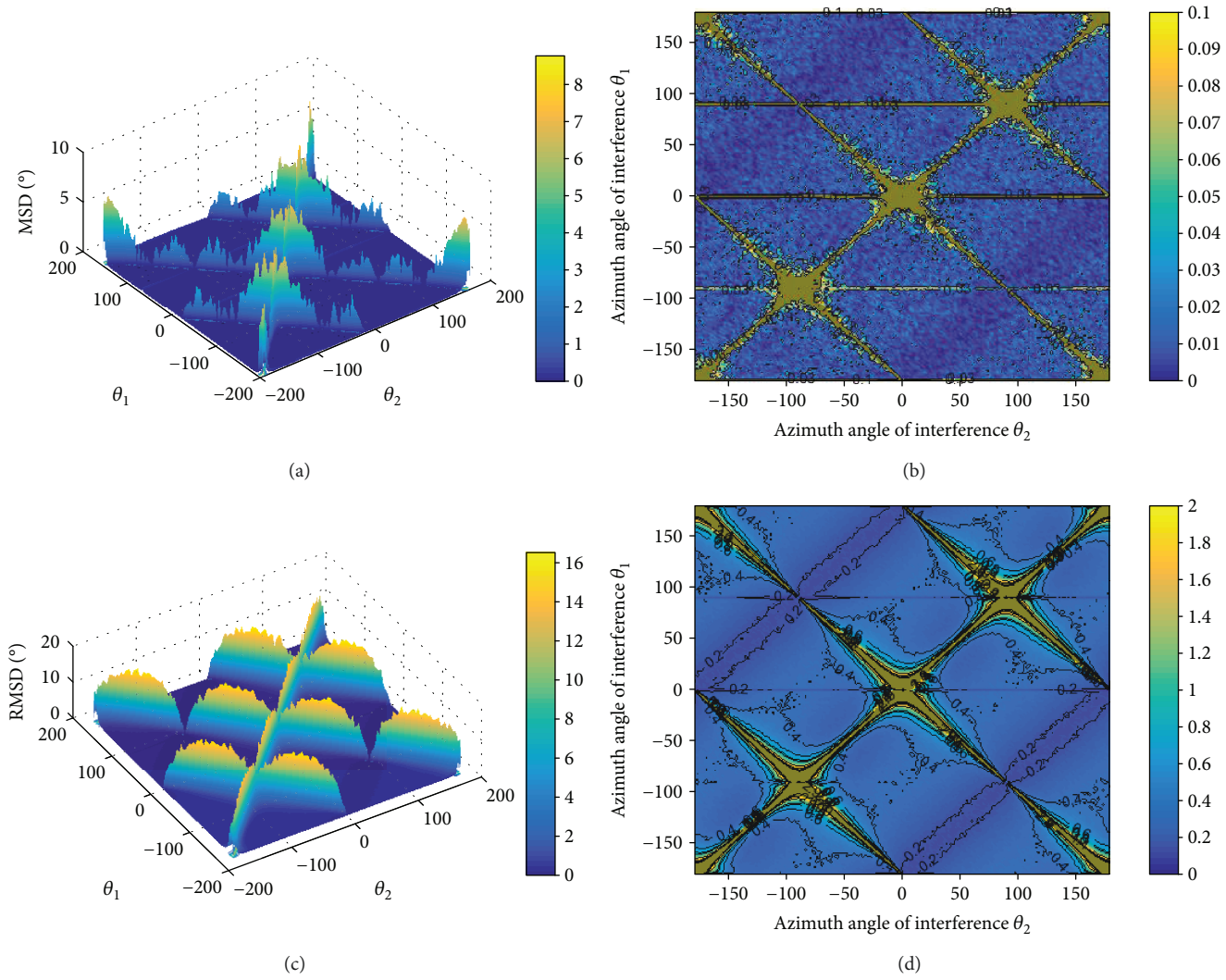

FIGURE 3: Performance of SAIE for different localizations of interference θ_1, at SNR = 5 dB and SIR = 10 dB. (a) MSD, (b) planform of (a), (c) RMSD, and (d) planform of (c).

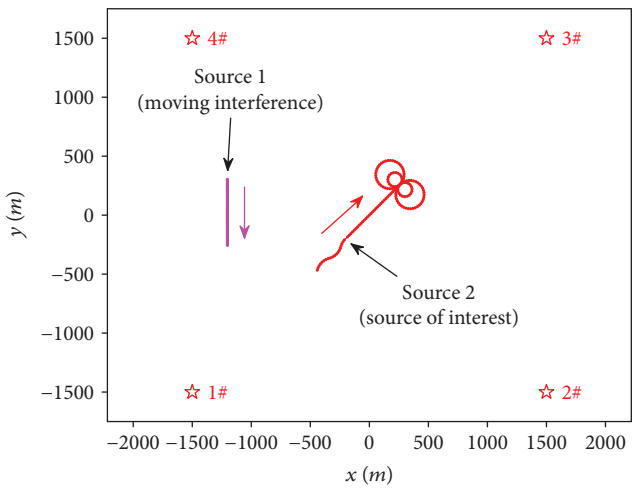

FIGURE 4: Distributed passive localization system.

The high-frequency acoustic source was 15 m deep in the water and transmitted a signal periodically. For SAIE1, source 1 was assumed as the interference and source 2 was taken as the source of interest. Alternatively, for SAIE2, source 1 was taken as the source of interest and source 2 was assumed as the interference. Note that CAIE can only obtain a single estimation of azimuth angle using the acoustic energy flux of both sources.

Figure 8(a) presents the estimation results from buoy 14#, with Figure 8(b) being a partial enlargement of (a). SAIE1 (black points) represents the results when the high-frequency acoustic source 1 is taken as the interference. For comparison, SAIE2 (cyan points) represents the results when the low-frequency acoustic source 2 is taken as the interference. The red points indicate the track of source 1 and the magenta points the track of source 2. As we can see from Figure 8(a), and more obviously from Figure 8(b), SAIE1 is able to estimate the azimuth angle accurately. As the acoustic energy flux comes from multiple sources, CAIE (blue points) is invalid. Related to the right panel of Figure 8(a), source 2 is closer to buoy 14# and has a stronger acoustic intensity.

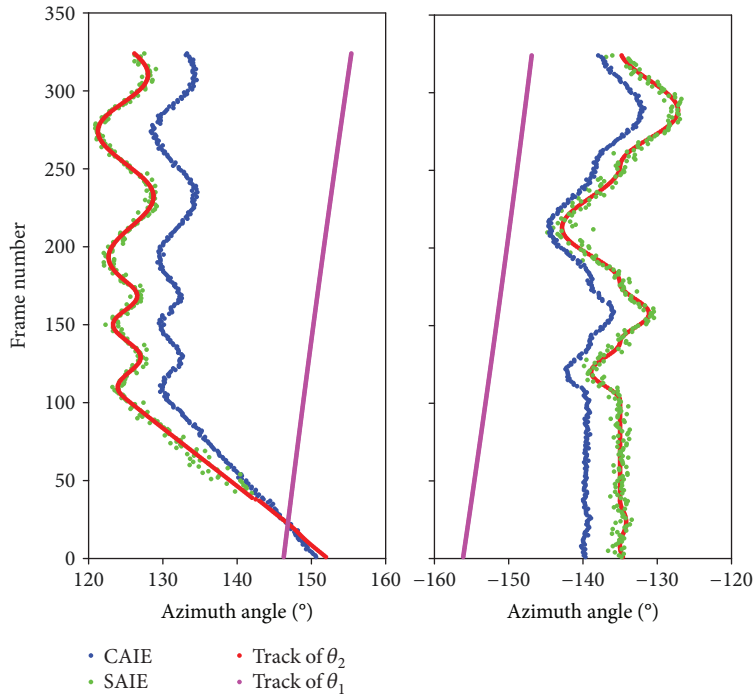

Figure 5: Results of azimuth angle estimation using buoy 2# (left panel) and buoy 3# (right panel).

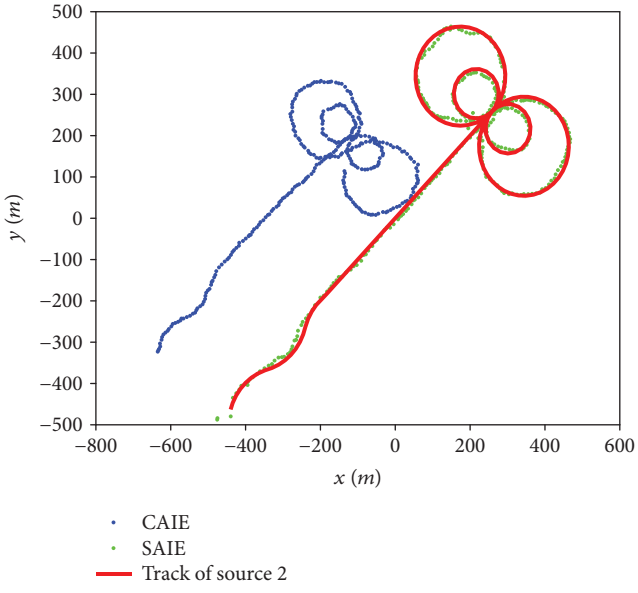

Figure 6: Tracking result from a typical distributed passive localization system.

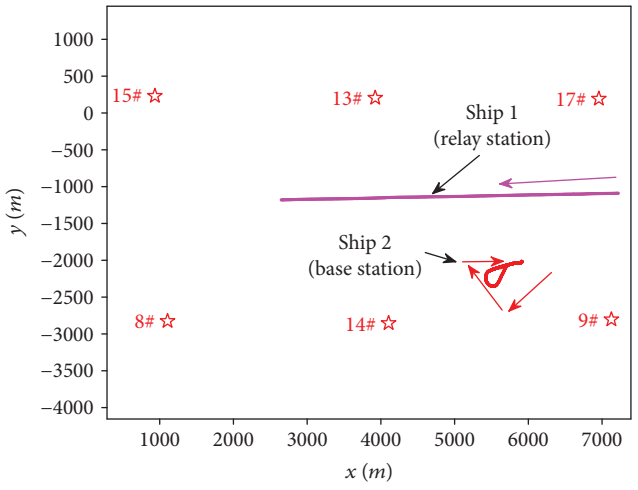

Figure 7: Distributed passive localization system in the sea trial.

Hence, the estimates of CAIE are closer to source 2. From 0 to 500 frames, source 1 keeps distant and source 2 approaches while the azimuth angles from two sources to buoy 14# remain close, known as the singular area. Since source 2 (source of interest) is closer to buoy 14#, SAIE1 is able to localize the azimuth angle accurately and consistently. Moreover, the performance of SAIE1 improves with source 2 approaching. Since source 1 (source of interest) is farther from buoy 14#, SAIE2 is heavily affected by the singular area and has a relatively high divergence. From 500 to 2000 frames, the performance of SAIE2 improves with source 1 leaving the singular area.

Figure 8(c) presents the estimation results from buoy 17#, with Figure 8(d) being a partial enlargement of (c). From 300 to 600 frames, the azimuth angles from two sources to buoy 14# remain close, known as the singular area. Since source 2 (source of interest) is farther from buoy 17#, the estimates of SAIE1 have a relatively high divergence due to the singular area. For SAIE2, source 1 (source of interest) moves far away from buoy 17# and the SNR decreases from 500 to 2000 frames. Hence, the performance of SAIE2 becomes worse.

The results of this sea trial show that SAIE can obtain accurate azimuth estimates of a source of interest, whereas

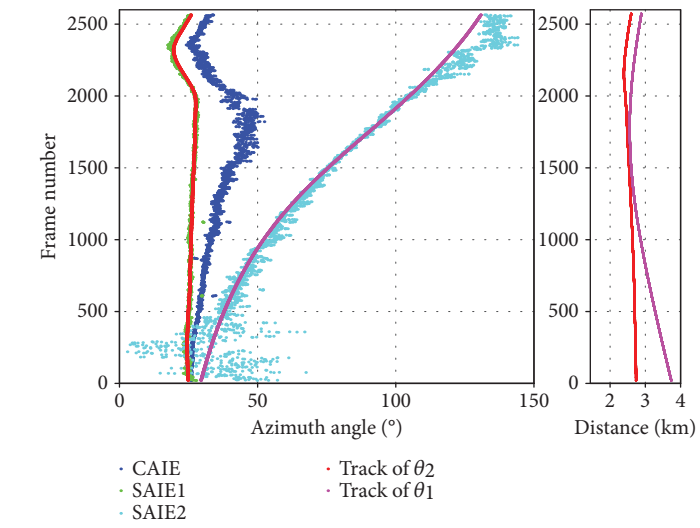

(a)

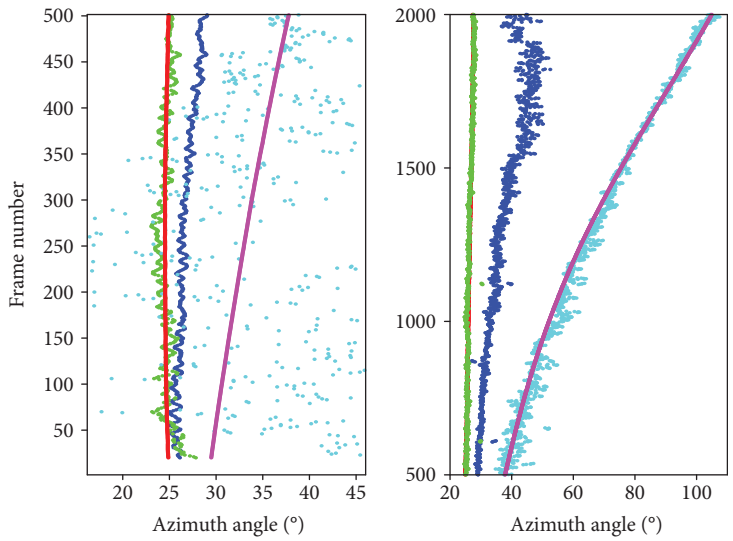

(b)

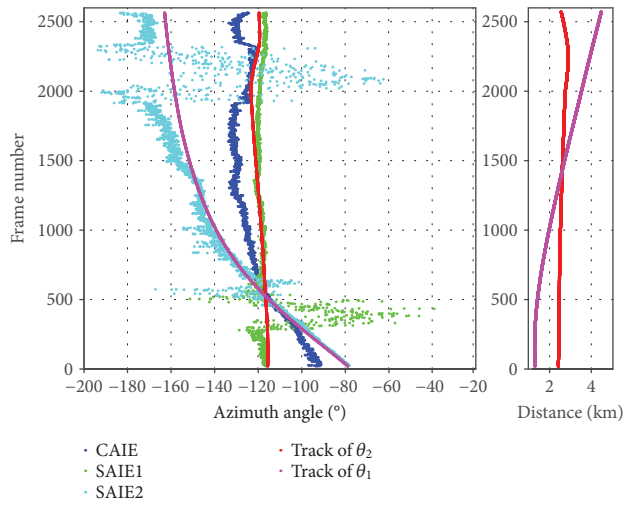

(c)

Figure 8: Continued.

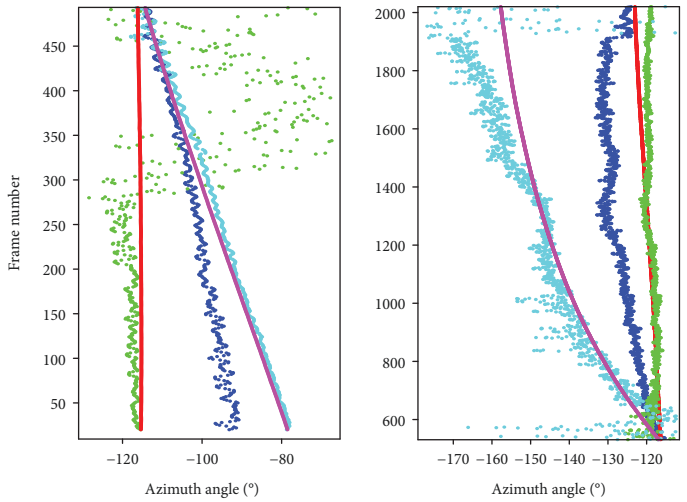

(d)

FIGURE 8: Experimental results of azimuth angle estimation by vector senor buoys in the sea trail. (a) Azimuth angle estimation by buoy 14# (left panel) and distances from source to buoy 14# (right panel); (b) partial enlarged view of (a) from 0 to 500 frames (left panel) and from 500 to 2000 frames (right panel); (c) azimuth angle estimation by buoy 17# (left panel) and distances from source to buoy 17# (right panel); (d) partial enlarged view of (c) from 0 to 500 frames (left panel) and from 500 to 2000 frames (right panel).

CAIE is invalid in the presence of background interference, with its performance being restricted by the SNR, SIR, and singular area, as discussed in Section 3.

5. Conclusion

We have proposed a method for estimating the azimuth angle in the presence of interference using a single vector hydrophone. Simulations and a sea trial have demonstrated the effectiveness of this method. The proposed method is able to estimate the azimuth angle accurately under conditions where the conventional CAIE method is invalid. Against a background of moving interference, the proposed method is applicable to a distributed passive localization system and is able to obtain the trajectory of the source. It does not require complex operations and allows a reduction in computational complexity.

Appendix

Derivation of the Steering Acoustic Energy Fluxes

Substituting the elements of the covariance matrix from (13), (14), (15), (16), (17), and (18) into (19) and (20), we have (A.3) and (A.4) below.

The steering azimuth angle is directed toward the estimated azimuth angle, given as $\theta = \widehat{\theta}_1$, and it is assumed in the neighborhood of the interference $\widehat{\theta}_1 \approx \theta_1$. Thus, we have

$$\mathcal{J}_x^2(\theta_1, \theta_2 \mid \theta)\big|_{\theta=\widehat{\theta}_1} \approx \left| \frac{P_2 \cos^2(\theta_2) - P_2 \cos(\theta_2) \cos\left(\widehat{\theta}_1\right)}{P_2 \sin^2(\theta_2) - P_2 \sin(\theta_2) \sin\left(\widehat{\theta}_1\right)} \right| = \left| \frac{\cos(\theta_2)\left[\cos(\theta_2) - \cos\left(\widehat{\theta}_1\right)\right]}{\sin(\theta_2)\left[\sin(\theta_2) - \sin\left(\widehat{\theta}_1\right)\right]} \right|, \tag{A.1}$$

$$\mathcal{J}_y^2(\theta_1, \theta_2 \mid \theta)\big|_{\theta=\widehat{\theta}_1} \approx \frac{P_2 \sin(\theta_2)\left[\cos(\theta_2) - \cos\left(\widehat{\theta}_1\right)\right]}{P_2 \cos(\theta_2)\left[\sin(\theta_2) - \sin\left(\widehat{\theta}_1\right)\right]} = \left| \frac{\sin(\theta_2)\left[\cos(\theta_2) - \cos\left(\widehat{\theta}_1\right)\right]}{\cos(\theta_2)\left[\sin(\theta_2) - \sin\left(\widehat{\theta}_1\right)\right]} \right|, \tag{A.2}$$

$$\mathcal{J}_x^2(\theta_1, \theta_2 \mid \theta) = \left| \frac{R_{22} - R_{12}\cos(\theta) - I_{nx}}{R_{33} - R_{13}\sin(\theta) - I_{ny}} \right| = \left| \frac{P_1 \cos^2(\theta_1) + P_2 \cos^2(\theta_2) + I_{nx} - [P_1 \cos(\theta_1)\cos(\theta) + P_2 \cos(\theta_2)\cos(\theta)] - I_{nx}}{P_1 \sin^2(\theta_1) + P_2 \sin^2(\theta_2) + I_{ny} - [P_1 \sin(\theta_1)\sin(\theta) + P_2 \sin(\theta_2)\sin(\theta)] - I_{ny}} \right|, \tag{A.3}$$

$$\mathcal{J}_y^2(\theta_1, \theta_2 \mid \theta) = \left| \frac{R_{23} - R_{13}\cos(\theta)}{R_{23} - R_{12}\sin(\theta)} \right| = \left| \frac{P_1 \cos(\theta_1)\sin(\theta_1) + P_2 \cos(\theta_2)\cos(\theta_2) - [P_1 \sin(\theta_1)\cos(\theta) + P_2 \sin(\theta_2)\cos(\theta)]}{P_1 \cos(\theta_1)\sin(\theta_1) + P_2 \cos(\theta_2)\sin(\theta_2) - [P_1 \cos(\theta_1)\sin(\theta) + P_2 \cos(\theta_2)\sin(\theta)]} \right|. \tag{A.4}$$

Data Availability

The data used to support the findings of this study are available from the corresponding author upon request.

Conflicts of Interest

The authors declare that they have no conflicts of interest.

Acknowledgments

The work described in this paper was funded by the National Natural Science Foundation of China (grant no. 51009042) and the Weapon Equipment Research Foundation of China (grant no. 9140C200203110C2003).

References

[1] G. L. D'Spain, W. S. Hodgkiss, and G. L. Edmonds, "The simultaneous measurement of infrasonic acoustic particle velocity and acoustic pressure in the ocean by freely drifting swallow floats," *IEEE Journal of Oceanic Engineering*, vol. 16, no. 2, pp. 195–207, 1991.

[2] Y. Song, K. T. Wong, and Y. L. Li, "Direction finding using a biaxial particle-velocity sensor," *Journal of Sound and Vibration*, vol. 340, pp. 354–367, 2015.

[3] C. H. Lee, H. R. L. Lee, K. T. Wong, and M. Razo, "The spatial-matched-filter beam pattern of a biaxial non-orthogonal velocity sensor," *Journal of Sound and Vibration*, vol. 367, pp. 250–255, 2016.

[4] X. Zhong, A. B. Premkumar, and H. Wang, "Multiple wide-band acoustic source tracking in 3-D space using a distributed acoustic vector sensor array," *IEEE Sensors Journal*, vol. 14, no. 8, pp. 2502–2513, 2014.

[5] A. Nehorai and E. Paldi, "Acoustic vector-sensor array processing," *IEEE Transactions on Signal Processing*, vol. 42, no. 9, pp. 2481–2491, 1994.

[6] D. Levin, E. A. P. Habets, and S. Gannot, "Maximum likelihood estimation of direction of arrival using an acoustic vector-sensor," *Journal of the Acoustical Society of America*, vol. 131, no. 2, pp. 1240–1248, 2012.

[7] M. Hawkes and A. Nehorai, "Acoustic vector-sensor beamforming and capon direction estimation," *IEEE Transactions on Signal Processing*, vol. 46, no. 9, pp. 2291–2304, 1998.

[8] H. Chen and J. Zhao, "Coherent signal-subspace processing of acoustic vector sensor array for DOA estimation of wideband sources," *Signal Processing*, vol. 85, no. 4, pp. 837–847, 2005.

[9] M. Hawkes and A. Nehorai, "Wideband source localization using a distributed acoustic vector-sensor array," *IEEE Transactions on Signal Processing*, vol. 51, no. 6, pp. 1479–1491, 2003.

[10] K. T. Wong and M. D. Zoltowski, "Closed-form underwater acoustic direction-finding with arbitrarily spaced vector-hydrophones at unknown locations," *IEEE Journal of Oceanic Engineering*, vol. 22, no. 4, pp. 649–658, 1997.

[11] A. Zhao, L. Ma, X. Ma, and J. Hui, "An improved azimuth angle estimation method with a single acoustic vector sensor based on an active sonar detection system," *Sensors*, vol. 17, no. 2, p. 412, 2017.

[12] P. Tichavsky, K. T. Wong, and M. D. Zoltowski, "Near-field/far-field azimuth and elevation angle estimation using a single vector hydrophone," *IEEE Transactions on Signal Processing*, vol. 49, no. 11, pp. 2498–2510, 2001.

[13] A. Zhao, L. Ma, J. Hui, C. Zeng, and X. Bi, "Open-lake experimental investigation of azimuth angle estimation using a single acoustic vector sensor," *Journal of Sensors*, vol. 2018, Article ID 4324902, 11 pages, 2018.

[14] Z. X. Yao, J. Y. Hui, P. Cai, and J. Yin, "A histogram approach of the azimuth angle estimation using a single vector hydrophone," *Applied Acoustics*, vol. 25, no. 3, pp. 161–167, 2006.

[15] W. Duan, R. Kirby, J. Prisutova, and K. V. Horoshenkov, "Measurement of complex acoustic intensity in an acoustic waveguide," *Journal of the Acoustical Society of America*, vol. 134, no. 5, pp. 3674–3685, 2013.

[16] T. Loyau and J. C. Pascal, "Statistical errors in the estimation of the magnitude and direction of the complex acoustic intensity vector," *Journal of the Acoustical Society of America*, vol. 97, no. 5, pp. 2942–2962, 1995.

[17] Z. X. Yao, J. Y. Hui, J. W. Yin, and J. Yang, "Four approaches to DOA estimation based on a single vector hydrophone," *The Ocean Engineering*, vol. 24, pp. 122–127, 2006.

[18] A. D. Pierce, *Acoustics: an Introduction to Its Physical Principles and Applications*, McGraw-Hill, 1981.

[19] S. Zhou and P. Willett, "Submarine location estimation via a network of detection-only sensors," *IEEE Transactions on Signal Processing*, vol. 55, no. 6, pp. 3104–3115, 2007.

[20] J. Luo, Y. Han, and L. Fan, "Underwater acoustic target tracking: a review," *Sensors*, vol. 18, no. 2, p. 112, 2018.